Bromine speciation and partitioning in slab-derived aqueous fluids and silicate melts and implications for halogen transfer in subduction zones

Marion Louvel[1,2], Carmen Sanchez-Valle[2], Wim J. Malfait[3], Gleb S. Pokrovski[4], Camelia N. Borca[5] and Daniel Grolimund[5]

[1]School of Earth Sciences, Bristol University, UK- BS81RJ, Bristol, United-Kingdom

[2]Institute for Mineralogy, WW-Universität Münster, D-48149, Münster, Germany

[3]Swiss Federal Laboratories for Materials Science and Technology EMPA, CH-8600, Dubendorf, Switzerland

[4]Groupe Métallogénie Expérimentale, Géosciences Environnement Toulouse (GET - UMR 5563), OMP-CNRS-IRD-University of Toulouse III Paul Sabatier, 31400 Toulouse, France

[5]Swiss Light Source, Paul Scherrer Institute, CH-5232, Villigen, Switzerland

Correspondence to: Marion Louvel (louvel@uni-muenster.de)

Abstract. Understanding the behavior of halogens (Cl, Br, and I) in subduction zones is critical to constrain the geochemical cycle of these volatiles and associatied trace metals, and to quantify the halogen fluxes to the atmosphere *via* volcanic degassing. Here, the partitioning of bromine between coexisting aqueous fluids and hydrous granitic melts and its speciation in slab-derived fluids have been investigated *in situ* up to 840 °C and 2.2 GPa by synchrotron X-ray fluorescence (SXRF) and x-ray absorption spectroscopy (XAS) in diamond-anvil cells. The partition coefficients $D^{f/m}_{Br}$ range from ~2 to ~15, with an average value of 6.7 ±3.6 (1σ) over the whole pressure-temperature *(P-T)* range, indicating a moderate Br enrichment in aqueous fluids, in agreement with previous work. EXAFS analysis further evidences a gradual evolution of Br speciation from hydrated Br ions $[Br(H_2O)_6]^-$ in slab dehydration fluids to more complex structures invoving both Na ions and water molecules, $[BrNa_x(H_2O)_y]$, in hydrous silicate melts and supercritical fluids released at greater depth (> 200 km). In denser fluids (ρ > 1.5 g.cm^{-3}), containing 60 wt% dissolved alkali-silicates and in hydrous $Na_2Si_2O_5$ melts (10 wt% H_2O), Br is found to be in a "salt-like" structure involving 6 nearest Na ions and several next-nearest O neighbors that are either from water molecules and/or the silicate network. Bromine (and likely chlorine and iodine) complexing with alkalis is thus an efficient mechanism for the mobilization and transport of halogens by hydrous silicate melts and silica-rich supercritical fluids. Our results suggest that both shallow dehydration fluids and deeper silicate-bearing fluids efficiently remove halogens from the slab in the sub-arc region, thus favoring an efficient transfer of halogens across subduction zones.

Keywords: Halogen cycle, speciation, partitioning, slab-derived fluid, subduction zone, silicate melt, diamond anvil cell.

1 Introduction

The fluxes of volatile elements (water, carbon, sulfur, and halogens) in subduction zones play a critical role in the Earth's chemical evolution; however, the mecanisms and extent of their transfer from slab components to the mantle wedge, the volcanic arc and, ultimately, the atmosphere remain poorly understood. Although halogens (F, Cl, Br and I) are rather minor volatiles compared to H_2O and CO_2, their effect on the physical and chemical properties of slab-derived fluids and arc magmas (*e.g.* phase equilibria, viscosity, density), as well as their ability to bind to trace elements and base metals (e.g., Au, Cu, Zn, Pb, REE) makes them key players in the chemical transfer in subduction zones and formation of ore deposits (e.g., Zellmer et al., 2015; Barnes et al., 2018). Furthermore, their emission to the troposphere and stratosphere at volcanic arc centres may have a significant environmental impact, including ozone depletion by Br (Bobrowski et al., 2003; von Glasow et al., 2009; Kutterolf et al., 2013). Constraining the halogen cycle in subduction zones is thus crucial for assessing their impact on the global atmospheric chemistry and climate.

In the last decade, new developments in quantification techniques on pore fluids, fluid inclusions and rocks as well as in detection methods for halogens species in volcanic gases enabled better estimates of halogen fluxes in subduction zones (Wallace, 2005; Pyle and Mather 2009; John et al., 2011; Kendrick et al., 2013; Kendrick et al., 2015; Chavrit et al., 2016; Barnes et al., 2018). For example, comparisons of the input from the subducted sediments, altered oceanic crust and serpentinized oceanic lithosphere to the output along volcanic arcs point to a significant imbalance between fluorine input and output, suggesting that a significant amount of F may be transferred to the deep mantle (Roberge et al., 2015; Grutzner et al., 2017). On the contrary, Cl, Br and I appear to be efficiently recycled up to the surface, either through shallow

loss of fluids to the fore-arc region (Br and especially I) or deeper release upon slab dehydration (especially Cl and Br, and to a lesser extent I) (Kendrick et al., 2018). Yet, the poor understanding of the transfer mechanisms and pathways of halogens limits the development of numerical models constraining the role of fluids in the global cycling of elements in subduction zones (Ikemoto and Iwamori, 2014; Kimura et al., 2016). There is for instance virtually no constraint on the amounts of residual halogens that may be stored in the dehydrated slab or lost to the continental crust through hidden hydrothermal activity and passive degassing. Similarly, current knowledge of halogens solubility and speciation in fluids and melts is mostly limited to pressures below 0.3 GPa (equivalent to ~10 km depth), which are relevant to volcanic degassing and ore deposit formation in the shallow crust (Webster, 1990; Métrich and Rutherford, 1992; Webster, 1992; Bureau et al., 2000; Signorelli and Carroll, 2002; Bureau and Métrich, 2003; Carroll, 2005; Evans et al., 2009; Cadoux et al., 2018), but not to slab dehydration or melting beneath arcs at far greater depth. Only recently, Bureau et al. (2010, 2016) reported fluid-melt partition coefficients for Br and I in the haplogranite-H_2O system up to 1.7 GPa while Cochain et al. (2015) investigated the speciation of Br in haplogranitic melts up to 7.6 GPa. Nevertheless, the effect of fluid chemistry on the speciation and partitioning of halogens at high pressures and temperatures (*P-T*) remains unknown in subduction zones. To fill this gap, we combined synchrotron X-ray fluorescence (SXRF) and X-ray absorption spectroscopy (XAS) measurements in a hydrothermal diamond-anvil cell (HDAC) to investigate Br fluid-melt partitioning and speciation in aqueous fluids and hydrous silicate melts that mimic the mobile phases released by the slab at sub-arc depths (Manning, 2004; Frezzotti and Ferrando, 2015). Bromine is employed here as an analog of chlorine amenable to SXRF and XAS studies through the diamond window of the HDAC due to its higher absorption edge energy (13.47 keV for

bromine K-edge compared to 2.82 keV for chlorine K-edge; Sanchez-Valle, 2013). Furthermore, among the halogens, bromine displays the closest behavior to chlorine in terms of solubility, partitioning and speciation in silicate melts, at least at shallow depth (Bureau et al., 2000, Bureau and Metrich, 2003; Wasik et al., 2005; Bureau et al., 2010; Cadoux et al., 2018). Bromine therefore represents the best analog of Cl for *in-situ* studies at high pressure (*P*) and high temperature (*T*) conditions. Our experimental results reveal systematic changes in Br speciation that reflect changes in fluid composition with depth; these new findings enable better constraints on the mechanisms controlling the transfer of halogens from the slab to arc magmas.

2 Methods

2.1 Starting materials

The speciation and fluid-melt partitioning experiments were conducted using 3 wt% NaBr aqueous solutions and synthetic sodium disilicate (NS2: $Na_2Si_2O_5$) or haplogranite (Hpg) glasses doped with 1 to 4 wt% Br as starting materials (Table 1). The 3 wt% NaBr aqueous solution was freshly prepared from distilled de-ionized water and analytical grade NaBr powder, sealed in tight containers and refrigerated until the experiments. The NS2 and Hpg glasses were synthesized in a piston-cylinder apparatus at 1200 °C and 0.5 GPa and 1.5 GPa, respectively, following the method described in Louvel et al. (2013). Briefly, reagent grade SiO_2 and Na_2SiO_3 were employed for the NS2 glasses whereas reagent grade SiO_2, Al_2O_3 and alkali-carbonates, K_2CO_3 and Na_2CO_3, were mixed for the haplogranite glass synthesis. Bromine was added as NaBr together with 3.3 wt% H_2O for the synthesis of the haplogranite glass to ensure complete melting and homogeneization of the sample at run conditions.

Major element (Si, Al, K and Na) contents and distribution in the glass were measured by by electron microprobe analyzer (EPMA) using a JEOL JXA-8200 microprobe with an

accelerating voltage of 15 keV, a 10 nA beam current and a defocused beam of 30 µm to avoid element migration during the analysis (Table 1). The probe was calibrated using wollastonite/quartz (Si), corundum (Al), aegirine (Na), K-feldspar (K), and counting time set to 40 s. The homogeneity of the glasses was confirmed by elemental profiles collected across the sample and by the absence of microscopic mineral phases. EPMA measurements of Br are hindered by i) the high ionization potential for the K-lines of Br resulting in low count rates; ii) the peak overlap between the L-lines of Br and the K-lines of Al; and iii) the lack of matrix-matched standards. To overcome these limitations, the concentration of Br in Hpg-Br2 glass sample was first determined by Rutherford Backscattering Spectroscopy (RBS) at the Department of Physics of ETH Zurich. This technique provides absolute elemental concentrations and is particularly appropriated for quantifying heavy elements in a light matrix as it is the case of Br in silicate glasses (Feldman and Mayer, 1986; Chu and Liu, 1996). A 3.5 mm diameter disk of Hpg-Br2 glass, mounted in epoxy and carbon-coated, was exposed to a 2 MeV ^{4}He ion beam. The concentration of Br in the sample was determined from the energy of the backscattered alpha particles $^{4}He^{2+}$, yielding a Br concentration of 0.96 ± 0.04 wt%, which is identical to the nominal Br concentration within analytical uncertainties (Table 1). This well-characterized sample was then used as a standard for Br analysis by EPMA and LA-ICPMS in the other glass samples (NS2 and Hpg-Br3 – Table 1). EPMA characterization of Br was conducted with an accelerating voltage of 25 keV, a 90 nA beam current and a defocused beam of 30 µm. The signal from Br (and Na) was carefully monitored during the measurements and found to be stable for these conditions. Br concentrations in NS2-Br1 were also cross-checked by LA-ICPMS analyses that were conducted using a 193-nm ArF excimer laser coupled with an ELAN 6100 DRC ICP quadrupole mass spectrometer (Heinrich et al., 2003) and a beam

diameter of 40 μm. All analyses were bracketed by measuring an external standard (NIST 610) to allow for linear drift correction, and the average SiO_2 and Br content determined by EPMA analysis for the Hpg-Br2 glass was used as the internal standard.

2.2 Hydrothermal diamond anvil cell experiments

All experiments were conducted in Bassett-type hydrothermal diamond-anvil cells (HDAC, Bassett et al., 1993) widely used for *in-situ* SXRF and XAS measurements on aqueous fluids and silicate melts up to 1000 °C and about 3 GPa (e.g., Borchert et al., 2009; Louvel et al., 2013, 2014). The HDAC were mounted with a thinner diamond (1.2-mm thick) on the detector side to reduce the X-ray path through the diamonds and widen the collection angle of the XAS analysis (Sanchez-Valle et al., 2004). This configuration permits i) to reduce the attenuation of the fluorescence X-rays in the anvil, and ii) to lower the fluorescence background arising from the Compton and Rayleigh scattering in the thick diamond anvils, hence increasing the signal to noise ratio and thus the overall quality of the analysis. The sample chamber, a 300-μm hole drilled in a 250-μm rhenium gasket compressed between the two diamond anvils, was heated externally with molybdenum wires wrapped around two tungsten carbide seats supporting the diamond anvils. Temperature was measured to within 2 °C with K-type thermocouples attached to each anvil, as close as possible to the sample chamber. The temperature gradient between thermocouples and the sample chamber was calibrated for each HDAC prior to experiments using the melting temperature at ambient pressure of S (115.4 °C), $NaNO_3$ (308.0 °C) and NaCl (800.5 °C). Overall, the *T* gradient remains <35 °C at the highest temperature reached (850 °C). Pressure was determined from the equation of state of the gold internal pressure standard (Jamieson et al., 1982) whose X-ray diffraction pattern was measured during the experiment.

Fluid-melt partitioning experiments were conducted by loading the sample chamber with a piece of Br-bearing Hpg glass and either pure H_2O or an aquous 3 wt% NaBr solution (Fig. 1). For the speciation measurements by XAS, loadings included either Br aqueous solutions, or a piece of Br-bearing NS2 or Hpg glass loaded together with de-ionized water. In all runs, a pellet of a mixture of Au and Al_2O_3 powders was added to be used for pressure calibration (Louvel et al., 2013; 2014). The volumetric proportions of glass and aqueous fluid in the different loadings were adjusted by adding double-side polished glass pieces of known dimensions (Fig. 1). Upon heating, the haplogranite melt-aqueous fluid system followed the classical phase transitions described in previous studies (Bureau and Keppler, 1999; Louvel et al., 2013), with initial hydrous melting recorded between 550 and 700 °C (Fig. 1B) and complete miscibility reached within the 700-850 °C range, depending on the pressure (Fig. 1C). In contrast, the NS2-H_2O system displayed distinct and rather unusual phase relations in the investigated *P-T* range (Fig. 1D-F): the NS2 glass first dissolved completely in the aqueous solution between 150 and 250 °C to produce a single fluid phase containing 30 to 60 wt% dissolved Na_2O and SiO_2 solutes, an analog for slab-derived so-called supercritical fluids (Fig. 1E). Upon further heating between 500 and 750 °C, the fluid unmixed into two phases, a hydrous melt and an aqueous fluid (Fig. 1F). This immiscibility gap remained open up to the highest temperatures reached with the HDAC (800-900 °C), as also previously observed for the haploandesite $Na_2Si_4O_9$-$Na_2(Si,Al)_4O_9$ join and the K_2O-SiO_2-H_2O system (Mysen and Cody, 2004).

The composition of the high-pressure fluids (wt% cations dissolved) and melts (wt% H_2O) was determined from available solubility studies (Table 2) as follows. The water content of haplogranite melts at equilibrium with aqueous fluids (Fig. 1B) was calculated from the water

174 solubility data for aluminosilicate melts reported by Mysen and Wheeler (2000) and extrapolated
175 to our experimental conditions. The composition of the aqueous fluid phase in equilibrium with
176 the haplogranite melt (*i.e.,* total silicates content including SiO_2, Al_2O_3, Na_2O and K_2O) was
177 estimated by extrapolating to the *P-T* conditions of our experiments the solubility data reported
178 for the albite-H_2O system between 0.20 and 0.84 GPa at 600 and 700 °C (Anderson and
179 Burnham, 1983), except for Run 4, for which the high pressure (1-2 GPa) solubility data of
180 Wolhers et al. (2011) were employed. Uncertainties in the calculated dissolved silicate content
181 mostly arise from the compositional differences between solubility models (albite) and our
182 experimental system (peralkaline haplogranite), but they cannot be rigorously quantified here
183 due to a lack of information on Si, Na, K and Al partitioning between silicate melts and water.
184 To account for potential uncertainties on calculated silicate contents in the fluid phase we thus
185 considered a 10% error on pressure values, which translates to an overall uncertainty of 20-22%
186 for all investigated conditions, except in Run 4 (Table 2). The compositions of the aqueous fluids
187 in the NS2-H_2O system were determined from the initial volumetric proportions of the NS2 glass
188 and the aqueous fluid loaded in the compression chamber. The mass of the glass was calculated
189 from its measured volume using a density of 2.52(5) g/cm^3 (Yamashita et al., 2008) and that of
190 the fluid determined from the volume left in the compression chamber (Fig. 1D). The amount of
191 water dissolved in the hydrous NS2 melt in equilibrium with the aqueous fluid at 700 °C and 0.4
192 GPa (Fig. 1F) was calculated from water solubility data in sodium silicate melts reported by
193 Mysen and Cody (2004). The overall error in the calculated bulk compositions is within 10% of
194 the total concentration value.
195
196 **2.3 *In-situ* SXRF and XAS measurements and data analysis**

197 The SXRF and XAS measurements were performed at the microXAS beamline (X05LA)
198 of the Swiss Light Source (SLS, Paul Scherrer Institute, Borca et al., 2009). Measurements at the
199 Br K-edge were conducted with an incident energy of 13.6 keV tuned by a Si(111) double crystal
200 monochromator and focused down to 5×8 (V×H) μm^2 size by a set of Rh-coated Kirkpatrick-
201 Baez mirrors. This configuration ensured a photon flux of 2×10^{11} photons per second at the
202 measurements conditions. The intensity of the incident beam was monitored throughout the
203 experiments using an Ar-filled micro-ion-chamber placed between the Kirkpatrick-Baez mirrors
204 and the HDAC. Before measurements, temperature was stabilized for about 30 min after each
205 heating stage to ensure that chemical equilibrium was achieved inside the cell (Louvel et al.,
206 2014). In the case of coexisiting melt and fluid, measurements were only performed when the
207 melt globule was stationary and bridging both diamonds (Fig. 1F). This configuration ensured
208 that spectra were only collected from pure phases (fluid or melt) thus avoiding any
209 contamination of the SXRF and XAS signals by the other coexisting phase. SXRF and XAS
210 spectra were collected in fluorescence mode in a forward scattering geometry with an energy
211 dispersive single-element silicon drift diode (SDD) detector (Ketek®, 139 eV resolution at Mn-K_α
212 = 5.89 keV) set at 22° from the incident beam in the horizontal plane (Sanchez-Valle et al., 2003;
213 Louvel et al., 2013; 2014). Angle-dispersive X-ray diffraction spectra were collected on the gold
214 pressure calibrant before and after XAS/SXRF measurements using a high-resolution CCD
215 camera set in transmission geometry. A microscope equipped with a video camera was used to
216 monitor the compression chamber during the heating and cooling cycles (Fig. 1).
217
218 2D-SXRF maps were acquired across the sample chamber to qualitatively monitor the
219 distribution of Br between the coexisting aqueous fluid and haplogranite melt (Fig. 1). Then, at

220 least three fluorescence spectra were collected from each phase to further determine the Br fluid-
221 melt partition coefficients $D_{Br}^{f/m}$ at each *P-T* condition (Table 2). Counting times were set to 100
222 or 300 s, depending on the signal intensity. Spectra were always recorded far away from the Au
223 pressure calibrant (Fig. 2) to suppress the contribution of the Au L_β line (11.442 keV) to the Br
224 K_α line (11.924 keV) used for the quantifications. Note that the Au L_β line was only observed in
225 the spectra when the beam spot was positioned within less than 5 μm away from the Au chip
226 (horizontal beam size 8 μm) thus demonstrating the well defined beam shape and appropriate
227 spatial resolution of the X-ray beam.
228 The fluid-melt partition coefficients, $D_{Br}^{f/m}$, which correspond to the ratio of Br concentration in
229 coexisting fluid (C_{Br}^{f}) and melt (C_{Br}^{m}) at each *P-T*, were derived from the integrated intensities of
230 the Br fluorescence emission line recorded in the fluid and melt, I_f and I_m, after normalization to
231 the incident beam intensity and counting times, and background removal with the Peakfit v4.12
232 software (SeaSolve Software-USA), following the method described in Louvel et al. (2014). This
233 method relies on the fixed geometry of the HDAC set-up and takes into account the different
234 composition, density (ϱ) and effective transmission (A) of the aqueous fluid and melt to
235 normalize the fluorescence signal and calculate $D_{Br}^{f/m}$ according to the equation:
236
237 $$D_{Br}^{f/m} = \frac{C_{Br}^{f}}{C_{Br}^{m}} = \frac{I_f}{I_m} \times \frac{A_m}{A_f} \times \frac{\rho_m}{\rho_f} \quad (1)$$
238
239 The standard deviation on the intensity ratios I_f/I_m is smaller than 10% (Table 2). The fluid and
240 melt densities were calculated for the relevant pressure, temperature and fluid or melt
241 compositions using density relations determined by *in situ* techniques for comparable fluid and

melt compositions by Mantegazzi et al. (2012) and Malfait et al. (2014) and assuming a 10% uncertainty on pressure determination and by propagating this error on the fluid and melt compositions. The effective transmission A_f *and* A_m, which accounts for the probability that the fluorescent radiation reaches the detector depending on phase composition, density and thickness of the sample at the incident energy, was calculated from the compositionally dependent attenuation lengths λ determined below and above the Br K-edge energy as a function of melt/fluid compositions and densities for all *P-T* conditions using the Hephaestus software (Ravel and Newville, 2005). The sample thickness *t* was set as an average of the thickness of the sample chamber after each run (~ 200 μm). A variation of the sample thickness by 50 μm induces a deviation smaller than 10 % on the absolute value of the A_m/A_f ratio. Note that the corrections in Eq. 1 significantly affect $D_{Br}^{f/m}$. Because the XRF intensities correlate with the Br concentration and the melts are denser than the fluids, the values for $D_{Br}^{f/m}$ are consistently higher than the I_f/I_m ratio itself (Table 2). Partition coefficients derived in this study are reported with 2σ uncertainty that takes into account the analytical uncertainty on the intensity ratios I_f/I_m and an extra 10 % error on pressure determination and its propagation on the fluid and melt compositions, densities and effective transmission.

XAS measurements were conducted on 3 wt% NaBr aqueous solution, 'solute-poor' fluids equilibrated with hydrous haplogranite melt (Fig. 1B), supercritical fluids containing different amounts of dissolved NS2 (Fig. 1E) and hydrous NS2 melt (Fig. 1F). XAS analyses on the haplogranite melt were precluded by the lower Br concentration of these melts (< 0.2 wt%). For each composition, 3 to 5 XAS spectra were collected with counting times of 1 second per point in the pre-edge region to 3 seconds in the XANES and EXAFS regions. The contribution of

265 Bragg reflections arising from the diamond anvils was avoided in the energy range of interest by
266 changing the orientation of the diamond anvil cell by 0.5 to 1° with respect to the incident X-ray
267 beam direction (Bassett et al., 2000). The edge position was calibrated using a pellet of NaBr and
268 no significant drift of the energy was observed during measurements. XAS spectra were also
269 collected at ambient conditions on ~ 200×200 μm^2 double-side polished section of the NS2 and
270 Hpg glasses.

271 Data reduction was performed using the Athena and Artemis packages (Ravel and
272 Newville, 2005) based on the IFEFFIT program (Newville, 2001). Averaged experimental
273 spectra were normalized to the absorption edge height and background removed using the
274 automatic background subtraction routine AUTOBK included in the Athena software. To
275 minimize the contribution of features at distances below the atom-atom contact distance, the R_{bkg}
276 parameter, which represents the minimum distance for which information is provided by the
277 signal, was set to 1.3 Å. For all spectra, the absorption energy E_0 was set to 13.474 keV, which
278 corresponds to the maximum of the first derivative of the absorption edge. Based on previous
279 studies of Br and Cl speciation in aqueous solutions and silicate glasses (Ayala et al., 2002;
280 D'Angelo et al., 1993; Evans et al., 2008; Ferlat et al., 2001; McKeown et al., 2011; Ramos et
281 al., 2000; Sandland et al., 2004; Stebbins and Du, 2002), our EXAFS analysis included the Br-O
282 and Br-Na scattering paths to describe the evolution of the local structure around Br from the
283 high *P-T* fluids to the hydrous melts and silicate glasses. Although Na cannot be easily
284 distinguished from Al or Si by EXAFS under our experimental conditions, the presence of
285 network cations in the nearest coordination shell of Br is deemed unlikely, as shown for Cl by
286 MAS-NMR and XAS studies (Evans et al., 2008; McKeown et al., 2011; Sandland et al., 2004;
287 Stebbins and Du, 2002). The theoretical back-scattering amplitudes, mean free-paths and phase-

shift functions for these paths were calculated with the FEFF6.0 *ab initio* code (Mustre de Leon et al., 1991) using an aqueous Br ion $[Br(H_2O)_6]^-$ with a mean Br-O distance of 3.37 Å and the NaBr salt crystallographic structure with a Br-Na distance of 2.98 Å (Deshpande, 1961; Makino, 1995). Multiple scattering within a linear Br···H-O cluster was also included to model the hydration shell around Br, with the H-O distance fixed to 1.0 Å (Silvestrelli and Parrinello, 1999; Soper and Benmore, 2008). The $\chi(k)$ EXAFS function were Fourier filtered over the 1.5-6.0 $Å^{-1}$ *k*-range for most spectra. For all samples, modelling of the EXAFS oscillations was performed using 4 variables: average coordination number (N), distance to nearest neighbor (R), Debye-Waller factor σ^2, and the energy shift ΔE (which is a non-structural parameter). The amplitude reduction factor S_0^2 was set to 1 based on previous fits of aqueous NaBr, KBr and $GaBr_3$ solutions (Da Silva et al., 2009; Ferlat et al., 2002). All fits were performed simultaneously with k-weighting of 1, 2 and 3 in order to decrease correlations between N and σ^2, and R and ΔE (Pokrovski et al., 2009a,b). The multi-electronic excitations (MEE) at 34 and 90 (± 1) eV above the Br K-edge (D'Angelo et al., 1993) were neglected as they did not significantly contribute to the EXAFS spectra. The variation of ΔE values between different fitted samples was less than ± 4 eV, further confirming the validity of the fitting procedure and the accuracy of the derived interatomic distances.

3 RESULTS AND DISCUSSION

3.1 Bromine partition coefficients in the haplogranite-fluid system

The distribution of Br between aqueous fluids and silicate melts at high *P-T* conditions has been constrained by measuring fluid-melt partition coefficients $D_{Br}^{f/m}$ from 592 to 840 °C and from 0.2 to 1.7 GPa in four experimental runs. For all investigated conditions, the $D_{Br}^{f/m}$

311 values are always higher than 1 (Table 2), confirming the preferential partitioning of Br into the
312 fluid phase, which is also qualitatively evident from the *in-situ* Br distribution maps reported in
313 Figure 2. The $D_{Br}^{f/m}$ values vary between 2.0 ±0.1 and 15.3 ±1.0, and fall within the range
314 reported in a previous HDAC study by Bureau et al. (2010) at similar *P-T* conditions (Fig. 3).
315 Our limited set of $D_{Br}^{f/m}$ values does not display any clear and systematic pressure, composition
316 or density dependence (Fig. 3B) as it would generally be expected for vapor-liquid and fluid-
317 melt equilibrium partitioning of elements, which postulates that a partition coefficient should
318 tend to 1 when approaching the critical point at which the compositions and densities of both
319 phases are identical by definition (e.g., Bureau and Keppler, 1999; Pokrovski et al., 2013 and
320 references therein). While such trend is indeed vaguely apparent for Runs 1 and 2, in which the
321 partition coefficients decrease with increasing *P-T*, Runs 3 and 4 do not show such trend (Fig.
322 3A). The lack of pressure-density trend and the apparent data scatter might be partially related to
323 larger uncertainties on the pressure calibration when employing the equation of state of gold at
324 low pressures. Yet, large differences between Br chemical speciation in the melt and fluid phases
325 (see section 3.2) may also contribute to the apparent data scatter, obscuring the simple water
326 activity-, density- or pressure-dependent partitioning trends as reported for vapor-liquid
327 partitioning (Pokrovski et al., 2013), and, ultimately, driving the system towards non-ideal, non-
328 Henrian behavior, as for instance reported for the fluid-melt partitioning of Cl under crustal
329 magmatic conditions (cf. data from Webster., 1992 in Fig. 3B). In this regard, the large $D_{Br}^{f/m}$ =
330 9.7 obtained at 1.7 GPa in Run 4, when the system should be close to miscibility and $D_{Br}^{f/m} \sim 1$
331 (Table 2, Fig. 3) may result, at least partly, from differences between the real fluid composition
332 and that estimated using available data (Wohlers et al., 2011), coupled with possible non-Henrian
333 effects, *i.e.*, ~ 2 wt% Br dissolved in the sample chamber compared to only ~0.5wt% for Runs 1

to 3. We further note that previous *in-situ* high *P-T* measurements of $D_{Br}^{f/m}$ (Bureau et al., 2010) also do not show clear *P-T* dependence for pressure > 0.6 GPa, e.g., $D_{Br}^{f/m}$ = 2.8-6.4 between 625-655 °C at 1.2 GPa. Thus, the combined effect of pressure, temperature and fluid and melt composition changes on Br fluid-melt partitioning should be more systematically investigated at $P > 0.2$ GPa.

Despite the current uncertainties, an important observation here is that the $D_{Br}^{f/m}$ values remain relatively small, 6.7 ±3.6 (1σ), over a wide range of *P-T* conditions. Assuming that the high *P-T* fluid/melt volumetric ratio is similar to the initial fluid/glass ratio for each run, we calculate between 0.04 and 0.2 wt% Br to be dissolved in the high *P-T* hydrous melts at run conditions. This estimation suggests that hydrous granitic melts have a capacity comparable to fluids to carry Br under subduction-zone *P-T* conditions and may thus contribute to the efficient transport of Br from the subducting slab to the mantle wedge and volcanic arc.

At lower-pressure conditions relevant to fore-arc or crustal processes (<0.2 GPa), our *in-situ* partition coefficients are slightly lower than those obtained from quench experiments (Fig. 3). For instance, Bureau et al. (2000) and Cadoux et al. (2018) reported average $D_{Br}^{f/m}$ of ~ 17-20 for albitic and rhyodacitic melts at 900 °C and 0.2 GPa, while we found $D_{Br}^{f/m}$ of ~ 5 at 800 °C and 0.2 GPa. The minimum $D_{Br}^{f/m}$ value from Cadoux et al. (2018) is ~ 9, which is close to our *in-situ* value. The small differences between our and the previous studies may stem from uncertainties in the pressure determination below 0.5 GPa in the HDAC, the quantification of Br by mass balance in Bureau et al. and Cadoux et al. (i.e. salt precipitates), or artifacts of the quench method resulting in the loss of Br to the aqueous phase upon cooling in those ex-situ

356 studies. Furthermore, slight differences in the melt composition and structure could also result in
357 different Br speciation (Louvel et al., 2020), favoring or not the incorporation of Br in the silicate
358 melt. The relatively low Br partition coefficients (< 20) compare favorably with those reported
359 for Cl in experiments conducted under Cl-undersaturated conditions (*i.e,* Webster., 1992 –
360 experiments with less <0.01 wt% Cl in quenched glass, reported as solid grey circles in Figure
361 3B). Nonetheless, comparison between these and our study underline that additional efforts are
362 yet required to quantifically assess the effect of halogens contents and density controls on Cl and
363 Br fluid-melt partitioning (see Dolejs and Zajacz, 2018 and Webster et al., 2018 for reviews).
364
365 **3.2 Speciation of bromine in aqueous fluids and silicate melts**
366 **3.2.1 Aqueous solutions and silicate glasses at room conditions**
367 The XANES and EXAFS spectra collected at ambient conditions from the 3 wt% NaBr
368 aqueous solution and Br-bearing silicate glasses are reported respectively in Figures 4 and 5,
369 together with data for a KBr aqueous solution from Ferlat et al. (2002). These spectra were
370 employed to validate the theoretical backscattering amplitude and phase shift functions for Br-O
371 and Br-Na scattering paths used in EXAFS modeling. The XANES spectrum of the 3 wt% NaBr
372 aqueous solution is characterized by an absorption edge at 13.474 keV and a white line that
373 peaks at 13.478 keV (Fig. 4). It displays close similarities to that of the KBr aqueous solution
374 from Ferlat et al. (2002) and overall resembles other alkali bromide aqueous solutions reported in
375 the literature (Wallen et al., 1997; Ferlat et al., 2001; Evans et al., 2007). The EXAFS spectra
376 from the KBr and NaBr aqueous solutions are accurately modeled with a hydration shell of 5.7 ±
377 0.8 and 5.9 ± 0.7 water molecules ($N_{Br..H-O}$) at a Br-O distance of 3.30 ± 0.03 and 3.37 ± 0.04 Å,
378 respectively (Table 3). Note that multiple-scattering paths from the linear Br···H-O cluster are

379 needed to accurately reproduce the experimental data; when only Br-O interactions are
380 considered, the model fails to reproduce the amplitude of the EXAFS oscillations unless an
381 unrealistic hydration shell of ~12 H_2O molecules is adopted. The structural parameters fitted for
382 the KBr aqueous solution from Ferlat et al. (2002) are, within errors, similar to those reported by
383 the authors. Together with the EXAFS fits of the NaBr aqueous solution, they confirm that Br
384 speciation in aqueous solution at room conditions is dominated by a six-fold coordinated
385 hydration shell with the H-O bond of the water molecule radially aligned towards the Br ion
386 (Ferlat et al., 2001; Ramos et al., 2000).

387 EXAFS spectra collected on NS2 and Hgp glasses at room conditions display distinct
388 oscillations, with a new feature at 2.2 $Å^{-1}$ in both glass samples and amplitudes nearly out of
389 phase at > 2 $Å^{-1}$ in *k*-space compared to the NaBr and KBr aqueous solutions (Fig. 6). Different
390 combinations of Br-Na and Br-O scattering paths were tested to constrain the local structural
391 environment of Br in the silicate glasses. Models considering individually either the Br-Na or Br-
392 O paths do not provide a reasonable fit of the EXAFS oscillations and the simultaneous
393 contribution of Br-Na and Br-O bond is required to reproduce the experimental spectra. The
394 EXAFS-derived parameters suggest that Br in NS2 and Hpg glasses is coordinated to an average
395 of 6 Na cations in the first shell at an average distance of 2.95 Å, and next-nearest 6 O neighbors
396 located at 3.4 Å (Table 3). The fitted Br-Na bond length is consistent, within errors, with
397 theoretical Br-Na distances in crystalline NaBr (2.987 Å, Deshpande, 1961) and is close to that
398 reported for aluminosilicate glasses in a previous study (Cochain et al., 2015), suggesting Br is
399 incorporated in the silicate glasses in a "salt-like" structure, similar to NaBr. The similarities
400 between the structural parameters fitted for anhydrous NS2 and hydrous Hpg (3.3 wt% H_2O)
401 glasses also suggest that the nearest environment of Br remains largely anhydrous in glasses

containing relatively low water contents and that the second O neighbors may be from the silicate network rather than more distant H_2O or OH groups. Attempts to include the effect of Br···H-O bonds in the fitting model by taking into account multiple scattering Br···H-O paths instead of Br-O correlations only resulted in a systematic decrease in the fit quality (higher *R*-factor). The sole difference between the two glasses is the presence of a pre-edge feature at ~13.468 keV in the haplogranite glass (Fig. 5). Such features have been attributed to the 1s to 4p electronic transitions in Br (Burattini et al., 1991) and reported in several covalently bonded and/or reduced Br-bearing compounds, including HBr, Br_2, and $CHBr_3$ (D'Angelo et al., 1993; Feiters et al., 2005). While Evans et al. (2007) suggested that this feature could arise from partial Br reduction in the presence of remaining carbon material in the sample from the synthesis, changes in the local site symmetry around Br could also contribute to the development of such feature. Recent HERFD-XAS measurements conducted on silicate glasses however demonstrate that this feature is absent in basaltic and andesitic glasses and hence, may be specific to the structure of granitic glass compositions (Louvel et al., 2020).

3.2.2 High *P-T* aqueous fluids and hydrous silicate melts

Bromine K-edge XANES spectra of high *P-T* aqueous fluids (3 wt% NaBr solution, fluids at equilibrium with haplogranite melt and water-dominated fluids containing < 50 wt% dissolved NS2) all share a shape very similar to that of the NaBr aqueous solution at room conditions, suggesting a similar local structure of Br in H_2O-dominated phases at elevated *P-T* (Fig. 4 and 5). Differences in the shape of the XANES spectra become more pronounced for the supercritical fluids with >50 wt% dissolved Si and Na and the hydrous NS2 melt (Fig. 4). Although the maximum of the white line remains at 13.478 keV, it broadens and decreases in

amplitude compared to the 3 wt% NaBr aqueous solution. Also, the first post-edge resonance is shifted toward either higher (13.504 keV) or lower (13.487 keV) energies compared to the aqueous fluids. These changes may be indicative of the progressive incorporation of Na in the local structure around Br. These modifications of Br coordination environment are also noticeable in the EXAFS oscillations (Fig. 5): while Br-bearing aqueous fluids mostly show a decrease of the amplitude of the oscillations with increasing *P*-*T*, they are shifted to higher distances (*i.e.* from 2.6 to 2.8 $Å^{-1}$ in *k*-space for the first oscillation) for the 60 wt% NS2 fluid. Moreover, the NS2 melt bears closer resemblance to the NS2 and Hpg glasses, sharing similar oscillations at 2.2 and 3.2 $Å^{-1}$.

The structural parameters derived from the quantitative EXAFS analysis are reported in Table 4. Comparably to room conditions, the EXAFS spectra of the NaBr aqueous solution at high pressure-temperature conditions are well matched by an octahedral hydration shell including multiple-scattering contributions from the Br···H-O cluster (Fig. 6). Br-O coordination numbers and distances are, respectively, 6.4 ± 1.1 and 3.40 ± 0.07 Å at 450 °C and 0.6 GPa, indicating the persistence of the 6-fold coordinated hydration shell up to high temperatures. This observation contrasts with results from a number of classical EXAFS studies performed at lower pressures (< 0.07 GPa at 450 ºC) that reported significant reduction in the number of water molecules around Br at supercritical conditions (Wallen et al., 1997; Da Silva et al., 2009). These differences are likely to reflect the differences in pressure (or fluid density), with higher pressures stabilizing the hydration shell around Br due to the increase in the solvent dielectric constant (Pan et al., 2013; Sverjensky et al., 2014), as also predicted for other ions such as Li^{+} (Jahn and Wunder, 2009) and Ti^{4+} (van Sijl et al., 2010) by molecular dynamics simulations. An exception to this trend are the experimental results of Mayanovic et al. (2001), who reported a

decrease by > 60% of the number of water molecules in the solvation shell of both Br aqua ions and $ZnBr_4^{2-}$ complexes in 1 m $ZnBr_2$ - 6 m NaBr aqueous solution from ambient conditions to 500 ºC and 0.5 GPa. The reason for this discrepancy is unclear at this state of our knowledge and additional studies on the speciation of Br in aqueous electrolytes will be necessary to explain the disagreement.

There are no significant changes in Br speciation in the aqueous fluids equilibrated with haplogranitic melts, which contain only few wt% of dissolved silicate components, and in fluids containing up to 30 wt% dissolved NS2 (Fig. 6; Table 4). The first noticeable changes are only found for fluids containing at least 50 wt% dissolved NS2, with a small decrease of the average Br coordination number ($N_{Br\ldots H\text{-}O}$) to ~ 4.7 compared to more dilute fluids (~ 6.0). While this value stays within errors from the other compositions, the reduction of the hydration shell might define the onset of Br-Na complexation with increasing amount of Na dissolved in the fluid. This hypothesis was tested by introducing a Br-Na contribution in the fitting model for the high temperature data, but this resulted in a decrease of the overall fit quality. The formation of Br-Na complexes and the partial dehydration of Br, however, becomes evident with further increase of the solute content to 60 wt% dissolved NS2 in the fluid (Table 4). For this composition, the best-fit model is consistent with the presence of ~ 3 Na atoms and 4 to 5 H_2O molecules (or OH groups) in the nearest environment of Br, at 480 °C and 1.5 GPa and 610 ºC and 2.2 GPa. In the NS2 hydrous melt (10 wt% H_2O), the number of Na neighbors further increases to ~ 6 whereas the number of oxygens remains similar to that of the 60 wt% NS2 fluid (~ 3.4). This increase in the number of Na neighbors compared to the 60 wt% NS2-bearing fluid suggests that the nearest environment of Br in silicate-rich fluids progressively approaches the local structure observed in the NS2 glass. Yet, the Br local environement remains hydrated, in contrast to the NS2 and Hpg

glasses. Based on results from FTIR and ^{29}Si NMR studies showing that molecular H_2O is favored in aluminosilicate and sodium silicate glasses as the amount of dissolved water increases (Stolper, 1982; Uchino et al., 1992; Xue and Kanzaki, 2004; Behrens and Yamashita, 2008), we suggest that molecular H_2O, rather than OH groups, would be present around Br in the hydrous NS2 melt. Moreover, we cannot exclude that distinct "fluid-like" $Br(H_2O)_6$ and "glass-like" $BrNa_6$ complexes coexist in the hydrous melt as $[yBr(H_2O)_6 + xBrNa_6]$ moieties, as the average signal of these structures could not be distinguished from $[BrNa_y(H_2O)_x]$ clusters by XANES or EXAFS. Although Br speciation could not be investigated in the hydrous haplogranite melt due to lower Br concentrations (< 0.2 wt%), the similarities between both XANES and EXAFS spectra of the Hpg and NS2 glasses (Fig. 4 and 5) allow us to anticipate a similar Br local environment in the haplogranite melt, dominated by alkali complexation.

4. Implications for the transport and recycling of halogens in subduction zones

The new partitioning and speciation data derived for bromine in the present study provide direct insights on the transport mechanisms of halogens (Cl, Br and I) in subduction zones. Our results suggest that the mobilization of Br (and likely Cl, Br and I) in subduction zones is affected by the chemistry of the slab-derived mobile phases. These phases, in turn, are essentially controlled by the slab composition and the depth of fluid extraction and hence, by the *P-T* conditions (Schmidt and Poli, 1998; Manning, 2004; Schmidt et al., 2004; Hermann et al., 2006; Bebout, 2007; Keppler, 2017). Figure 6 illustrates a gradual transition of Br speciation from hydrated species $[Br(H_2O)_6]^-$ to $[BrNa_x(H_2O)_y]$ clusters with various stoichiometries (or mixture of $[Br(H_2O)_6]$ and $BrNa_6$ moieties) as the fluid composition evolves from diluted aqueous fluids such as those released by continuous metamorphic dehydration of the slab (< 15 wt% dissolved

494 solutes, Manning, 2004; Rustioni et al., 2019) to Si/Na-rich supercritical fluids that form owing
495 to enhanced solubility of silicate minerals at depth and/or granitic melts produced by fluid-
496 assisted melting of subducted sediments (Hermann et al., 2006; Skora and Blundy, 2010). The
497 increasing similarities in the local structure of Br in aqueous fluids containing large amounts of
498 dissolved alkali-silica (> 12.5 wt% Na) and the hydrous melts (Fig. 6) is consistent with the
499 progressive decrease in the Br fluid-melt partition coefficients ($D_{Br}^{f/m}$) with *T* increase observed
500 in this study in each separated runs (Fig. 3). Sodium complexation with Br is thus an efficient
501 mechanism that enables not only aqueous fluids but also supercritical fluids and hydrous melts to
502 carry significant amounts of Br at depth.

503 General similarities between Cl, Br and I speciation in aqueous solutions and silicate
504 glasses (Evans et al., 2008; McKeown et al., 2011,2015; Shermann et al., 2010) suggest that the
505 speciation and partitioning trends found in our study for Br may extend to Cl and I. Therefore,
506 while early dehydration fluids should release large amounts of halogens to the fore-arc and the
507 mantle wedge (100 – 200 km depth), hydrous slab melts and supercritical fluids play a critical
508 role in recycling the residual halogens dragged by the subducting slabs to greater depths. Such
509 efficient recycling, where most of the Cl and Br subducted is transfered to the mantle wedge and
510 ultimately returned to the surface through arc magmatism, is further supported by recent
511 quantification of halogens in subducted sediments, serpentinites and altered oceanic crust. Mass
512 balance calculations indeed show a close match, within errors, between worldwide influx to the
513 mantle wedge, ~ 13-15 $\times 10^3$ kt/yr Cl and 5-70 kt/yr Br, and calculated outflux as HCl and HBr at
514 volcanic arcs, ~ 3-22 $\times 10^3$ kt/yr Cl and 5-15 kt/yr Br (Barnes et al., 2018; Chavrit et al., 2016;
515 Kendrick et al., 2013; Pyle and Mather, 2009). In comparison, iodine degassing at volcanic arcs
516 is less well constrained, making it more difficult to assess its fate in the subduction factory (e.g.,

517 Bureau et al., 2016). The small imbalances remaining between Cl and Br input and output fluxes
518 may arise from difficulties in quantifying halogen loss to the fore-arc and crustal hydrothermal
519 systems. Recent reports of halogens enrichment in oceanic islands basalts (Barnes et al., 2018;
520 Hanyu et al., 2019; Kendrick et al., 2017) also point to the subduction of a noticeable fraction of
521 F, Cl, Br and I to greater depth, to an extent that is yet to be quantified. Additional in-situ
522 experiments, like those presented here, may help better constrain the mecanisms of halogen
523 transfert and partitioning at depth, which are inaccessible to direct observation.
524
525 **5. Conclusions**
526 *In-situ* SXRF and XAS have been applied to quantify Br fluid-melt partition coefficients
527 and speciation in aqueous fluids, supercritical fluids and hydrous silicate melts up to 840 °C and
528 2.2 GPa. Above all, our experimental results demonstrate how changes in speciation, from
529 hydrated ions in aqueous fluids to 'salt-like' structures in hydrous melts, may facilitate the
530 uptake of high amounts of Cl, Br and, probably, I by subduction zone fluids, regardless of their
531 composition. Significant efforts are, however, still needed to accurately quantify halogen cycling
532 from the surface to the deep Earth and back. Especially, new experiments investigating the
533 solubility of halogens in subduction zone fluids and the capacity of high-pressure minerals (e.g.,
534 micas, Ti-clinohumite, apatite, and carbonates) to incorporate these elements are still necessary
535 to evaluate the amounts of halogen that may be returned to the volcanic arc or retained in the
536 slab.
537 **Acknowledgements:** This work was supported by the Swiss National Science Foundation
538 (grants 200021-120575 and 200020-132208 to CSV) and by the Swiss Academy of Sciences
539 (SATW) and the Ministères des Affaires étrangères et européennes (MAEE) et de

l'Enseignement Supérieur et de la Recherche (MESR) through the Partenariat Hubert Curien (PHC). We thank M. Doebeli and J. H. Seo for conducting the RBS and LA-ICPMS analysis, respectively. The Paul Scherrer Institute (PSI) and the Swiss Light Source (SLS) are acknowledged for providing beamtime for the experiments. Two anonymous reviewers and the Topical Editor N. Malaspina are thanked for their help in improving the clarity of the article.

References

Anderson, G. M. and Burnham, C. W.: Feldspar solubility and the transport of aluminum under metamorphic conditions. Am. J. Sci. 283, 283-297, 1983.

Ayala, R., Martinez, J. M., Pappalardo, R. R., Saint-Martin, H., Ortega-Blake I. and Sanchez-Marcos, E.: Development of first-principles interaction model potentials. An application to the study of the bromide hydration. J. Chem. Phys. **117**, 10512, 2002.

Barnes, J., Manning, C.E., Scambelluri, M. and Selverstone, J.: The behaviour of halogens during subduction-zone processes. In D.E. Harlov and L. Aranovich (eds.), The Role of Halogens in Terrestrial and Extraterrestrial Geochemical Processes, Springer Geochemistry, 545-590, 2018.

Bassett, W. A., Shen, A. H., Bucknum, M., and Chou, I. M.: A New Diamond-Anvil Cell for Hydrothermal Studies to 2.5 GPa and from – 190 °C to 1200 °C. Rev. Sci. Instrum. 64, 2340-2345, 1993.

Bassett, W. A., Anderson, A. J., Mayanovic, R. A., and Chou, I.-M.: Hydrothermal diamond anvil cell for XAFS studies of first-row transition elements in aqueous solution up to supercritical conditions. Chem. Geol. 167, 3-10, 2000.

Bebout, G. E.: Metamorphic chemical geodynamics of subduction zones. Earth Planet. Sc. Lett. 260, 373-393, 2007.

Behrens, H. and Yamashita, S.: Water speciation in hydrous sodium tetrasilicate and hexasilicate melts: Constraint from high temperature NIR spectroscopy. Chem. Geol. 256, 306-315, 2008.

565 Bobrowski, N., Honninger, G., Galle, B., and Platt, U.: Detection of bromine monoxide in a volcanic
566 plume. Nature 423, 273-276, 2003.
567 Borca, C. N., Grolimund, D., Willimann, M., Meyer, B., Jefimovs, K., Vila-Comamala, J., and David, C.:
568 The microXASbeamline at the Swiss Light Source: towards nano-scale imaging. J. Phys. Conf. Ser.
569 186, 1-3, 2009.
570 Borchert, M., Wilke, M., Schmidt, C., and Rickers, K.: Partitioning and equilibration of Rb and Sr
571 between silicate melts and aqueous fluids. Chem. Geol. 259, 39-47, 2009.
572 Burattini, E., D'Angelo, P., Giglio, E. and Pavel, N.V.: EXAFS study of probe molecules in micellar
573 solutions. J. Phys. Chem. 95, 7880-7886, 1991.
574 Bureau, H. and Keppler, H.: Complete miscibility between silicate melts and hydrous fluids in the upper
575 mantle: experimental evidence and geochemical implications. Earth Planet. Sc. Lett. 165, 187-196,
576 1999.
577 Bureau, H. and Métrich, N.: An experimental study of bromine behaviour in water-saturated silicic melts.
578 Geochim. Cosmochim. Ac. 67, 1689-1697, 2003.
579 Bureau, H., Keppler, H., and Metrich, N.: Volcanic degassing of bromine and iodine: experimental
580 fluid/melt partitioning data and applications to stratospheric chemistry. Earth Planet. Sc. Lett. 183,
581 51-60, 2000.
582 Bureau, H., Foy, E., Raepsaet, C., Somogyi, A., Munsch, P., Simon, G., and Kubsky, S.: Bromine cycle in
583 subduction zones through in situ Br monitoring in diamond anvil cells. Geochim. Cosmochim. Ac.
584 74, 3839-3850, 2010.
585 Bureau, H., Auzende A-L., Marocchi, M., Raepsaet, C., Munsch, P., Testemale, D., Mezouar, M.,
586 Kubsky, S., Carriere, M., Ricolleau, A. and Fiquet, G.: Modern and past volcanic degassing of
587 iodine. Geochim. Cosmochim. Ac. 173, 114-125, 2016.
588 Cadoux, A., Iacono-Marziano, G., Scaillet, B., Aiuppa, A., Mather, T.A., Pyle, D.M., Deloule, E.,
589 Gennaro, E. and Paonita, A.: The role of melt composition on aqueous fluid vs. silicate melt
590 partitioning of bromine in magmas. Earth Planet. Sc. Lett. 498, 450-463, 2018.

591 Carroll, M. R.: Chlorine solubility in evolved alkaline magmas. Annals of Geophysics 48, 619-631, 2005.
592 Chavrit, D., Burgess, R., Sumino, H., Teagle, D.A.H., Droop, G., Shimizu, A. and Ballentine, C.J.: The
593 contribution of the hydrothermal alteration of the ocean crust to the deep halogen and noble gas
594 cycles. Geochim. Cosmochim. Ac. 183, 106-124, 2016.
595 Chu, W. K. and Liu, J. R.: Rutherford backscattering spectrometry: Reminiscences and progresses. Mat.
596 Chem. Phys. 46, 183-188, 1996.
597 Cochain, B., Sanloup, C., de Grouchy, C., Crepisson, C., Bureau, H., Leroy, C., Kantor, I., Irifune, T.:
598 Bromine speciation in hydrous silicate melts at high pressure. Chem. Geol. 404, 18-26, 2015.
599 D'angelo, P., Dicicco, A., Filipponi, A., and Pavel, N. V.: Double-electron excitation channels at th Br K-
600 edge of HBr and Br_2. Phys. Rev. A 47, 2055-2063, 1993.
601 Da Silva, C., Proux, O., Hazemann, J. L., James-Smith, J., Testemale, D., and Yamaguchi, T.:. X-ray
602 absorption spectroscopy study of solvation and ion-pairing in aqueous gallium bromide solutions at
603 supercritical conditions. J. Mol. Liq. 147, 83-95, 2009
604 Deshpande, V.: Thermal Expansion of Sodium Fluoride and Sodium Bromide. Acta Crystallogr. 14, 794,
605 1961.
606 Dolejs, D. and Zajacz, Z.: Halogens in silicic magmas and their hydrothermal systems. In D.E. Harlov
607 and L. Aranovich (eds.), The Role of Halogens in Terrestrial and Extraterrestrial Geochemical
608 Processes, Springer Geochemistry, 431-543, 2018.
609 Evans, K. A., Mavrogenes, J., and Newville, M.: The effect of CO_2 on the speciation of bromine in low-
610 temperature geological solutions: an XANES study. J. Synchrotron Radiat. 14, 219-226, 2007.
611 Evans, K. A., Mavrogenes, J. A., O'Neill, H. S., Keller, N. S., and Jang, L. Y.: A preliminary
612 investigation of chlorine XANES in silicate glasses. Geochem. Geophy. Geosy. 9. Q10003,
613 doi:10.1029/2008GC002157, 2008.
614 Evans, K.A., Gordon, R.A., Mavrogenes, J.A. and Tailby, N.: The effect of CO_2 on the speciation of
615 RbBr in solution at temperatures to 579 °C and pressures to 0.26 GPa. Geochim. Cosmochim. Ac.
616 73, 2631-2644, 2009.

Feldman, L. C. and Mayer, J. W.: Fundamentals of Surface and Thin Film Analysis. Prentice Hall. pp 352, 1986.

Ferlat, G., San Miguel, A., Jal, J. F., Soetens, J. C., Bopp, P. A., Daniel, I., Guillot, S., Hazeman, J. L., and Argoud, R.: Hydration of the bromine ion in a supercritical 1 : 1 aqueous electrolyte. Phys. Rev. B 63, 2001.

Ferlat, G., San Miguel, A., Jal, J. F., Soetens, J. C., Bopp, P. A., Hazemann, J. L., Testemale, D., and Daniel, I.: The quest for ion pairing in supercritical aqueous electrolytes. J. Mol. Liq. 101, 127-136, 2002.

Frezzotti, M.L. and Ferrando, S.: The chemical behavior of fluids released during deep subduction based on fluid inclusions. Am. Mineral. 100, 352-377, 2015.

Grutzner, T., Klemme, S., Rohrbach, A., Gervasoni, F. and Berndt, J.: The role of F-clinohumite in volatiles recycling processes in subduction zones. Geology 45, 443-446, 2017.

Hanyu, T., Shimizu, K., Ushikubo, T., Kimura, J-I., Chang, Q., Hamada, M., Ito, M., Iwamori, H. and Ishikawa, T.: Tiny droplets of ocean island basalts unveil Earth's deep chlorine cycle. Nat. Commun. 10:60. https://doi.org/10.1038/s41467-018-07955-8, 2019.

Heinrich, C. A., Pettke, T., Halter, W. E., Aigner-Torres, M., Audétat, A., Günther, D., Hattendorf, B., Bleiner, D., Guillong, M., and Horn, I.: Quantitative multi-element analysis of minerals, fluid and melt inclusions by laser-ablation inductively-coupled-plasma mass-spectrometry. Geochim. Cosmochim. Ac. 67, 3473-3497, 2003.

Hermann, J., Spandler, C., Hack, A. and Korsakov, A.V.: Aqueous fluids and hydrous melts in high-pressure and ultra-high pressure rocks: Implications for element transfer in subduction zones. Lithos 92, 399-417, 2006.

Ikemoto, A. and Iwamori, H.: Numerical modeling of trace element transportation in subduction zones : implications for geofluid processes. Earth Planets Space 66:26, 1-10, 2014.

641 Jahn, S. and Wunder, B.: Lithium speciation in aqueous fluids at high P and T studied by ab initio
642 molecular dynamics and consequences for Li-isotope fractionation between minerals and fluids.
643 Geochim. Cosmochim. Ac. 73, 5428-5434, 2009.
644 Jamieson, J. C., Fritz, J. N., and Manghnani, M. H.: Pressure measurement at high temperature in X-ray
645 diffraction studies: gold as a primary standard in High-Pressure Research in Geophysics, pp 27-48.
646 Center for Academic Publishing, Tokyo, 1982.
647 John, T., Scambelluri, M., Frische, M., Barnes, J. D., and Bach, W.: Dehydration of subducting
648 serpentinite: Implications for halogen mobility in subduction zones and the deep halogen cycle.
649 Earth Planet. Sc. Lett. 308, 65-76, 2011.
650 Kendrick, M.A., Honda, M., Pettke, T., Scambelluri, M., Phillips, D. and Giuliani, A.: Subduction zone
651 fluxes of halogens and noble gases in seafloor and forearc serpentinites. Earth Planet. Sc. Lett. 365,
652 86-96, 2013.
653 Kendrick, M.A., Honda, M. and Vanko, D.A.: Halogens and noble gases in Mathematician Ridge meta-
654 gabbros, NE Pacific: implication for oceanic hyrothermal root zones and global volatile cycles.
655 Contrib. Mineral. Petr. 170:43, 2015.
656 Kendrick, M.A., Hemond, C., Kamenetsky, V.S., Danyushevsky, L., Devey, C.W., Rodemann, T.,
657 Jackson, M.G. and Perfit, M.R.: Seawater cycled throughout Earth's mantle in partially
658 serpentinized lithosphere. Nat. Geosci. 10, 222-229, 2017.
659 Kendrick, M.A., Scambelluri, M., Hermann, J. and Padron-Navarta, J.A.: Halogens and noble gases in
660 serpentinites and secondary peroditites: Implications for seawater subduction and the origin of
661 mantle neon. Geochim. Cosmochim. Ac. 235, 285-304, 2018.
662 Keppler, H.: Fluids and trace element transport in subduction zones. Am. Mineral. 102, 5-20, 2017.
663 Kimura, J-I., Gill, J-B., Skora, S., van Keken, P.E. and Kawabata, H.: Origin of geochemical mantle
664 components: Role of subduction filter. Geochem. Geophy. Geosy. 17, 3289-3325, 2016.

665 Louvel, M., Sanchez-Valle, C., Malfait, W.J., Testemale, D. and Hazemann, J-L.: Zr complexation in
666 high pressure fluids and implications for the mobilization of HFSE in subduction zones. Geochim.
667 Cosmochim. Ac. 104, 281-299, 2013.
668 Louvel, M., Sanchez-Valle, C., Malfait, W.J., Testemale, D. and Hazemann, J-L.: Constraints on the
669 mobilization of Zr in magmatic-hydrothermal processes in subduction zones from in situ fluid-melt
670 partitioning experiments. Am. Mineral. 99, 1616-1625, 2014.
671 Louvel, M., Cadoux, A., Brooker, R., Proux, Olivier and Hazemann, J-L.: New insights on Br speciation
672 in volcanic glasses and structural controls on halogens degassing. *In press,.Am. Mineral., 2020,*
673 10.2138/am-2020-7273
674 Makino, Y.: Correlation between Pseudopotential Radii and Interatomic Distance and Evaluation of Bond
675 Characters for Transition and Lanthanide Elements. J. Alloy. Compd. 227, 18-27, 1995.
676 Manning, C. E.: The chemistry of subduction-zone fluids. Earth Planet. Sc. Lett. 223, 1-16, 2004.
677 Mayanovic, R. A., Anderson, A. J., Bassett, W. A., and Chou, I. M.: Hydrogen bond breaking in aqueous
678 solutions near the critical point. Chem. Phys. Lett. 336, 212-218, 2001.
679 McKeown, D. A., Gan, H., Pegg, I. L., Stolte, W. C., and Demchenko, I. N.: X-ray absorption studies of
680 chlorine valence and local environments in borosilicate waste glasses. J. Nucl. Mater. 408, 236-
681 245, 2011.
682 McKeown, D.A., Muller, I.S. and Pegg, I.L.: Iodine valence and local environments in borosilicate waste
683 glasses using X-ray absorption spectroscopy. J. Nucl. Mater. 456, 182-191, 2015.
684 Mustre de Leon, J., Rehr, J. J., Zabinsky, S. I., and Albers, R. C.: Ab initio curved-wave X-ray-absorption
685 fine structure. Phys. Rev. B 44, 4146-56, 1991.
686 Mysen, B. O. and Cody, G. D.: Solubility and solution mechanism of H_2O in alkali silicate melts and
687 glasses at high pressure and temperature. Geochim. Cosmochim. Ac. 68, 5113-5126, 2004.
688 Mysen, B.O. and Wheeler, K.: Solubility behavior of water in haploandesitic melts at high pressure and
689 high temperature. Am. Mineral. 85, 1128-1142, 2000.
690 Newville, M.: EXAFS analysis using FEFF and FEFFIT. J. Synchrotron Radiat. 8, 96-100, 2001.

691 Pan, D., Spanu, L., Harrison, B., Sverjensky, D.A. and Galli, G.: Dielectric properties of water under
692 extreme conditions and transport of carbonates in the deep Earth. PNAS 110, 6646-6650, 2013.
693 Pokrovski, G. S., Tagirov, B. R., Schott, J., Hazemann, J. L., and Proux, O.: A new view on gold
694 speciation in sulfur-bearing hydrothermal fluids from in situ X-ray absorption spectroscopy and
695 quantum-chemical modeling. Geochim. Cosmochim. Ac. 73, 5406-5427, 2013.
696 Pokrovski, G. S., Tagirov, B. R., Schott, J., Bazarkina, E. F., Hazermann, J. L., and Proux, O.: An in situ
697 X-ray absorption spectroscopy study of gold-chloride complexing in hydrothermal fluids. Chem.
698 Geol. 259, 17-29, 2009b.
699 Pokrovski G.S., Borisova A.Y., Bychkov A.Y.: Speciation and transport of metals and metalloids in
700 geological vapors. Book chapter 6 in: Thermodynamics of Geothermal Fluids (eds. A. Stefánsson,
701 T. Driesner, P. Bénézeth). Rev. Miner. Geochem. 76, 165-218, 2013.
702 Poli, S. and Schmidt, M.W.: Petrology of subducted slabs. Annu. Rev. Earth Planet. Sci. 30, 207-235,
703 1998
704 Pyle, D. M. and Mather, T. A.: Halogens in igneous processes and their fluxes to the atmosphere and
705 oceans from volcanic activity: A review. Chem. Geol. 263, 110-121, 2009.
706 Ramos, S., Barnes, A. C., Neilson, G. W., Thiaudiere, D., and Lequien, S.: The hydration structure of Br-
707 from anomalous x-ray diffraction. J. Phys.-Condens. Mat. 12, A203-A208, 2000.
708 Ravel, B. and Newville, M.: ATHENA, ARTEMIS, HEPHAESTUS: data analysis for X-ray absorption
709 spectroscopy using IFEFFIT. J. Synchrotron Radiat. 12, 537-541, 2005.
710 Roberge, M., Bureau, H., Bolfan-Cassanova, N., Frost, D.J., Raepsaet, C., Surble,S., Khodja, H.,
711 Auzende, A-L. and Fiquet, G.: Is the transition zone a deep reservoir for fluorine? Earth Planet. Sc.
712 Lett. 429, 25-32, 2015.
713 Rustioni, G., Audetat, A. and Keppler, H.: Experimental evidence for fluid-induced melting in subudction
714 zones. Geochem. Perspect. Lett, 11, 49-54, 2019.
715 Sanchez-Valle, C.: Structure and thermodynamics of subduction zone fluids from spectroscopic studies.
716 Rev. Mineral. Geochem. 76, 265-309, 2013.

717 Sanchez-Valle, C., Martinez, I., Daniel, I., Philippot, P., Bohic, S., and Simionovici, A.: Dissolution of
718 strontianite at high P-T conditions: An in-situ synchrotron X-ray fluorescence study. Am. Mineral.
719 88, 978-985, 2003.
720 Sanchez-Valle, C., Daniel, I., Martinez, I., Simionovici, A., and Reynard, B.: Progress in quantitative
721 elemental analyses in high P-T fluids using synchrotron x-ray fluorescence (SXRF). J. Phys.-
722 Condens. Mat. 16, S1197-S1206, 2004.
723 Sandland, T. O., Du, L. S., Stebbins, F., and Webster, J. D.: Structure of Cl-containing silicate and
724 aluminosilicate glasses: A ^{35}Cl MAS-NMR study. Geochim. Cosmochim. Ac. 68, 5059-5069,
725 2004.
726 Schmidt, M.W., Vielzeuf, D. nad Auzanneau E.: Melting and dissolution of subducting crust at high
727 pressures: the key role of white mica. Earth Planet. Sc. Lett. 228, 65-84, 2004.
728 Sherman, D.M.: Metal complexation and ion association in hydrothermal fluids: insights from quantum
729 chemistry and molecular dynamics. Geofluids 10, 41-57, 2010.
730 Signorelli, S. and Carroll, M. R.: Experimental study of Cl solubility in hydrous alkaline melts:
731 constraints on the theoretical maximum amount of Cl in trachytic and phonolitic melts. Contrib.
732 Mineral. Petr. 143, 209-218, 2002.
733 Silvestrelli, P. L. and Parrinello, M.: Structural, electronic, and bonding properties of liquid water from
734 first principles. J. Chem. Phys. 111, 3572-3580, 1999.
735 Skora, S. and Blundy, J.: High-pressure hydrous phase relations of radiolarian clay and implications for
736 the involvement of subducted sediment in arc magmatism. J. Pet. 51, 2211-2243, 2010.
737 Soper, A. K. and Benmore, C. J.: Quantum Differences between Heavy and Light Water. Phys. Rev. Lett.
738 101, 065502-1-4, 2008.
739 Stebbins, J. F. and Du, L. S.: Chloride ion sites in silicate and aluminosilicate glasses: A preliminary
740 study by Cl-35 solid-state NMR. Am. Mineral. 87, 359-363, 2002.
741 Stolper, E.: Water in silicate glasses: An infrared spectroscopic study. Contrib. Mineral. Petr. 81, 1-17,
742 1982.

743 Sverjensky, D.A., Harrison, B. and Azzolini, D.: Water in the deep Earth : The dielectric constant and the
744 solubilities of quartz and corundum to 60 kb and 1200 C. Geochim. Cosmochim. Ac. 129, 125-145,
745 2014.
746 Uchino, T., Sakka, T., Ogata, Y., and Iwasaki, M.: Mechanism of hydration of sodium-silicate glass in a
747 steam environment - Si^{29} NMR and ab initio molecular-orbital studies. Journal of Physical
748 Chemistry 96, 7308-7315, 1992.
749 van Sijl, J., Allan, N. L., Davies, G. R., and van Westrenen, W.: Titanium in subduction zone fluids: First
750 insights from ab initio molecular metadynamics simulations. Geochim. Cosmochim. Ac. 74,
751 2797-2810, 2010.
752 Von Glasow, R., Bobrovski, N. and Kern, C.: The effects of volcanic eruptions on atmospheric chemistry.
753 Chem. Geol. 263, 131-142, 2009.
754 Wallace, P. J.: Volatiles in subduction zone magmas: concentrations and fluxes based on melt inclusion
755 and volcanic gas data. J. Volcanol. Geoth. Res. 140, 217-240, 2005.
756 Wallen, S. L., Palmer, B. J., Pfund, D. M., Fulton, J. L., Newville, M., Ma, Y. J., and Stern, E. A.:
757 Hydration of bromide ion in supercritical water: An X-ray absorption fine structure and molecular
758 dynamics study. J. Phys. Chem. A 101, 9632-9640, 1997.
759 Wasik, A., Dingwell, D.B., Courtial, P. and Hess, K.: Viscosity and chemical diffusion of halogens in
760 silicate melts: implications for volcanic degassing. Eos Trans. AGU 86 (52) Fall Meet. Suppl.,
761 Abstract V21E-0667, 2005.
762 Webster, J. D.: Partitioning of F between H_2O and CO_2 fluids and topaz rhyolite melt - Implications for
763 mineralizing magmatic-hydrothermal fluids in F-rich granitic systems. Contrib. Mineral. Petr. 104,
764 424-438, 1990.
765 Webster, J. D.: Water Solubility and Chlorine Partitioning in Cl-Rich Granitic Systems - Effects of Melt
766 Composition at 2 kbar and 800 °C. Geochim. Cosmochim. Ac. 56, 679-687, 1992.

Webster, J.D., Baker, D.R. and Aiuppa, A.: Halogens in mafic and intermediate-silica content magmas. In D.E. Harlov and L. Aranovich (eds.), The Role of Halogens in Terrestrial and Extraterrestrial Geochemical Processes, Springer Geochemistry, 307-430, 2018.

Wohlers, A., Manning, C.E. and Thompson, A.B.: Experimental investigation of the solubility of albite and jadeite in H_2O, with paragonite + quartz at 500 and 600 °C, and 1-2.25 GPa. Geochim. Cosmochim. Ac. 75, 2924-2939, 2011.

Xue, X. Y. and Kanzaki, M.: Dissolution mechanisms of water in depolymerized silicate melts: Constraints from H-1 and Si-29 NMR spectroscopy and ab initio calculations. Geochim. Cosmochim. Ac. 68, 5027-5057, 2004.

Yamashita, S., Behrens, H., Schmidt, B. C., and Dupree, R.: Water speciation in sodium silicate glasses based on NIR and NMR spectroscopy. Chem. Geol. 256, 231-241, 2008.

List of Tables and Figure captions:

Table1. Synthesis conditions and chemical compositions of the $Na_2Si_2O_5$ (NS2) and haplogranite (Hpg) glasses employed as starting materials in this study.

Table 2: Bromine fluid-melt partition coefficients at different P-T conditions. Calculated fluid and melt compositions and densities are also reported.

Table 3. Structural parameters derived from Br K-edge EXAFS analysis for the reference aqueous solutions and silicate glasses at ambient conditions.

Table 4: Br K-edge EXAFS analysis of experimental high P-T fluids with various compositions.

Figure 1. Microphotographs of the compression chamber of the HDAC showing the Haplogranite - H_2O (A, B, C) and NS2 - H_2O (D, E, F) systems at the indicated pressure and temperature conditions. Images are taken through the diamond along the X-ray path. A) Haplogranite glass and 3 wt% NaBr aqueous solution at room conditions; B) globulus of hydrous silicate melt in equilibrium with the aqueous fluid; C) supercritical liquid (single fluid phase); D) NS2 glass and 3 wt% NaBr aqueous solution at room conditions; E) supercritical liquid (low temperature supercriticality); F) hydrous NS2 melt coexisting with aqueous fluid (high temperature subcriticallity).

Figure 2. 2D-SXRF Br K_α intensity maps of Run 1 showing the distribution of Br between coexisting aqueous fluid and haplogranite melt at different P-T conditions. The fluid:glass ratio refers to the wt

fraction calculated from the volumetric proportions of loaded glass and sample chamber. The white dashed line delimits the edge of the Re gasket.

Br-enriched phases appear in red and yellow, Br-depleted areas in blue and green. At the beginning of the experiment (A), all the Br is concentrated in the glass. After the glass melts (B), Br strongly partitions into the fluid phase ($D_{Br}^{f/m}$ = 8.07 ±0.79). As temperature increases, the Br concentration in the melt increases while the Br concentrations in the fluid decreases (C). At 821°C - 0.9GPa, the I_f/I_m ratio appears homogeneous as the Br concentrations per volume are almost similar (I_f/I_m = 1.3 ±0.1). However, per weight, Br still partitions preferentially into the fluid ($D_{Br}^{f/m}$ = 2.02 ±0.14).

Figure 3. Evolution of the Br partition coefficients $D_{Br}^{f/m}$ with (A) increasing temperature at different pressure conditions and (B) density ratio of coexisting fluids and melts for given *P*-*T*. The different symbols and colors account for separate experimental runs involving different glass proportions. The errors reported on $D_{Br}^{f/m}$ take into account analytical uncertainties on the SXRF signal intensities in fluid and melt and an additional uncertainty of 10% on pressure determination. The Br and Cl fluid/melt partition coefficients from Bureau et al. (2000, 2010), Cadoux et al. (2018) and Webster (1992) are shown for comparison. For Cadoux et al., note that both average values from several experiments ($D_{Br}^{f/m}$ = 20.2 ±1.2) and minimum value for a single experiment ($D_{Br}^{f/m}$ = 8.6) are reported. For Webster (1992), the solid and dotted symbols are for experiments were Cl in glass was < 0.01 wt% and 0.01-0.03 wt%, respectively.

Figure 4. Normalized Br K-edge XANES spectra collected on Br-bearing silicate glasses, aqueous fluids and hydrous silicate melts at various pressure and temperature conditions. Spectra are offset for clarity. The vertical dashed line is a visual guide to appreciate phase shifts. The black arrow shows the pre-edge

838 feature in the haplogranite glass spectrum corresponding to the 1s to 4p transition in Br (Burattini et al.,
839 1991).
840
841 **Figure 5.** Normalized k^1-weighted EXAFS oscillations of the investigated Br-bearing samples (black
842 solid lines) and corresponding least-square fits (blue dashed lines). Spectra are off-set vertically for
843 clarity. The pressure and temperature conditions and the compositions are reported right to each spectrum.
844 The dashed lines underline the shift of EXAFS oscillations with change in composition.
845
846 **Figure 6.** Evolution of bromine coordination numbers with oxygen (from H_2O molecules) and sodium
847 ($N_{Br\cdots H\text{-}O}$ and $N_{Br\text{-}Na}$) as a function of fluid composition (*i.e*, the weight fraction of NS2 dissolved in the
848 fluid) along the NaBr aqueous solution – NS2 join. The gray field shows the detection limit (DL) for Br-
849 Na complexes, which corresponds to the maximum Br-Na coordination number ($N_{Br\text{-}Na}$) determined for
850 3wt% NaBr aqueous solution at ambient conditions and 450 °C (DL < 1.5 atoms).
851

852 **Table 1.**

Sample	Synthesis conditions T (°C)	P(GPa)	Br[1] (wt%)	Na_2O[2] (wt%)	SiO_2[2] (wt%)	Al_2O_3[2] (wt%)	K_2O[2] (wt%)	H_2O[3] (wt%)	ASI[4]	Analytical method
NS2-Br1	1200	0.5	4.01 4.10	32.0	63.9					EMPA LA-ICPMS
Hpg-Br2	1200	1.5	- 0.96	7.1	74.1	9.2	3.7	3.3	0.57	EMPA RBS
Hpg-Br3	1200	1.5	0.89	7.4	75.0	9.4	3.8	3.3	0.57	EMPA

853
854
855 **Notes: EMPA =** Electron Microprobe Analyses; **LA-ICPMS =** Laser-ablation Inductively Couple Plasma Mass Spectrometry;
856 **RBS** = Rutherford Backscattering Spectroscopy.
857 [1]Standard deviations (1σ) are 0.04 wt% for RBS analysis, 0.3 wt% for LA-ICPMS and 0.03 wt% for EMPA analysis.
858 [2]Average from 10 to 25 analyses performed on each glass composition. Standard deviations (1σ) are < 0.1 wt% for Na_2O, Al_2O_3 and
859 K_2O and < 0.3 wt% for SiO_2.
860 [3]Nominal H_2O concentration (not analyzed).
861 [4]Aluminum Saturation Index ASI = $\frac{Al_2O_3}{Na_2O+K_2O}$ (in moles).
862
863
864
865
866
867
868
869
870
871
872
873
874
875
876
877
878
879
880
881

Table 2.

X_g [1]	T (°C)	P (GPa) [2]	H_2O in melt (wt%) [3]	Melt density ρ_m [4]	Transmission in melt T_m	Silicates in fluid (wt%) [5]	Fluid density ρ_f [7]	Transmission in fluid T_f	I_{Br}^{f} / I_{Br}^{m}	$D_{Br}^{f/m}$
Haplogranite – H_2O										
Run 1										
0.76	592	0.7	7.1 ±0.8	2.24	0.66	2.5 ±0.5	0.94	0.96	4.9	**8.1** ±1.6
	694	0.8	7.7 ±0.9	2.23	0.67	5.3 ±1.2	0.97	0.95	2.6	**4.2** ±0.4
	821	0.9	8.0 ±1.0	2.23	0.67	10.3 ±2.3	0.99	0.95	1.3	**2.0** ±0.2
Run 2										
0.82	645	0.9	9.1 ±1.1	2.22	0.67	5.5 ±1.1	1.02	0.95	10.0	**15.3** ±2.0
	710	1.1	11.1 ±1.4	2.20	0.68	11.1 ±2.4	1.09	0.94	5.4	**7.9** ±1.0
	840	0.9	7.9 ±1.0	2.23	0.67	10.8 ±2.4	0.98	0.95	2.8	**4.4** ±0.6
Run 3										
0.72	610	1.2	13.3 ±1.7	2.18	0.69	7.7 ±1.6	1.13	0.95	4.6	**6.4** ±0.6
	730	0.65	6.0 ±0.7	2.25	0.66	3.9 ±0.9	0.88	0.96	2.3	**4.1** ±0.8
	800	0.2	2.4 ±0.2	2.26	0.64	0.7 <0.1	0.49	0.98	1.6	**4.8** ±0.6
Haplogranite – 3 wt% NaBr aqueous solution										
Run 4										
0.70	740	1.7	19.5 ±2.8	2.11 ±0.02	0.72	12.8 ±0.8 [6]	1.20	0.94	7.2	**9.7** ±1.2
Error (unless indicated)		±0.1		±0.01	±0.07		±0.04	±0.01	±0.04-0.43	

Notes:

[1] Initial weight fraction of glass in the loading.

[2] Maximum **estimated** uncertainty on pressure **for the calculations** were of 10%.

[3] H_2O solubility in the haplogranite melt calculated from the solubility data of Mysen and Wheeler (2000).

[4] Melt density (in $g.cm^{-3}$) calculated as a function of P-T conditions and melt composition using Malfait et al. (2014).

[5] Solubility of silicate components (SiO_2, Na_2O, Al_2O_3 and K_2O)in the aqueous fluid coexisting with haplogranite melt calculated from the albite solubility data of Anderson and Burnham (1983).

[6] Silicate solubility in the aqueous fluid estimated from Wohlers et al. (2011) for P > 1.2 GPa.

[7] Fluid density (in $g.cm^{-3}$) calculated as a function of P-T conditions from the data of Mantegazzi et al. (2013)

894

895

896 **Table 3.**

Composition	Oxygen (O)			Sodium (Na)			
Aqueous solutions[1]							
	$N_{Br\cdots H\text{-}O}$	$R_{Br\cdots H\text{-}O}$ (Å)	σ^2 (Å^2)				*R-factor*
3 wt% NaBr-H_2O	5.9 ±0.7	3.37 ±0.04	0.02				0.04
2.3 wt% KBr-H_2O.[3]	5.7 ±0.8	3.30 ±0.03	0.02				0.06
Silicate glasses[2]							
	$N_{Br\text{-}O}$	$R_{Br\text{-}O}$ (Å)	σ^2 (Å^2)	$N_{Br\text{-}Na}$	$R_{Br\text{-}Na}$ (Å)	σ^2 (Å^2)	*R-factor*
NS2 glass	5.2 ±2.4	3.45 ±0.09	0.02	5.3 ±1.8	2.99 ±0.09	0.03	0.25
Haplogranite glass	6.1 ±3.6	3.39 ±0.03	0.02	5.9 ±1.8	2.94 ±0.03	0.03	0.21

897

898 **Notes:** N = Br coordination number ($N_{Br\text{-}O}$ or $N_{Br\text{-}Na}$); R = Br-neighbor (Na or O) mean distance (Å); σ^2 = squared Debye-Waller
899 factor (Å^2); *R-factor* = goodness of the fit; $S_0^2 = 1$;
900 [1] Hydration shell (Br···H-O)
901 [2] Br coordinated to oxygens from the silicate network (next-nearest coordination shell).
902 [3] Ferlat et al. (2002), 0.2m KBr-H_2O for comparison.
903

Table 4.

Composition	T (°C)	P (GPa)	$N_{Br\cdots H\text{-}O}$	$R_{Br\cdots H\text{-}O}$ (Å)	σ^2 (Å^2)	$N_{Br\text{-}Na}$	$R_{Br\text{-}Na}$ (Å)	σ^2 (Å^2)	*R-factor*
3 wt% NaBr aqueous solution									
	25	0	5.9 ± 0.7	3.37 ±0.04	0.02	bdl[1]			0.04
	320	0.2	6.3 ± 1.8	3.36 ±0.05	0.04	bdl			0.17
	450	0.6	6.4 ±1.1	3.40 ±0.07	0.05	bdl			0.19
Br-bearing aqueous fluids									
1.2 wt% Hpg[3]	475	1	5.4 ±0.9	3.33 ±0.03	0.05	bdl			0.13
5 wt% Hpg	680	0.8	5.7 ±1.1	3.30 ±0.04	0.06	bdl			0.12
0.6 wt% Hpg	750	0.2	5.0 ±1.6	3.33 ±0.06	0.06	bdl			0.30
30 wt% NS2[2]	190	n.d.	6.7 ±1.4	3.38 ±0.03	0.04	bdl			0.14
	320	n.d.	5.7 ±1.4	3.37 ±0.09	0.04	bdl			0.22
50 wt% NS2	580	1.1	4.7 ±1.5	3.35 ±0.15	0.04	bdl			0.25
Br-bearing melt-like fluids									
60 wt% NS2	480	1.5	3.6 ±1.5	3.47 ±0.05	0.01	2.5 ±1.2	3.10 ±0.06	0.01	0.23
	610	2.2	4.8 ±2.4	3.45 ±0.05	0.03	2.6 ±0.9	3.06 ±0.06	0.03	0.20
NS2 melt (10 ±1 wt% H_2O)	710	0.4	3.4 ±1.6	3.36 ±0.03	0.02	6.6 ±2.1	2.91 ±0.03	0.05	0.24

Notes: N = Br coordination number (dissociate as $N_{Br\cdots H\text{-}O}$ and $N_{Br\text{-}Na}$); R = Br-neighbor mean distance (Å); σ^2 = squared Debye-Waller factor (Å^2); *R-factor* = goodness of the fit; $S_0^2 = 1$.

[1]bdl = below detection limit. Detection limit corresponds to the maximum Br-Na coordination number determined for 3 wt% NaBr aqueous solution at ambient conditions.

[2]wt% NS2 indicates the amount of dissolved NS2 in the single phase fluid calculated from the mass of H_2O and NS2 glass.

[3]wt% Hpg refers to the amount of dissolved silicate in the fluid coexisting with haplogranite melt calculated as in Table 2.

Errors in temperature and pressure are ±2 ºC and 10%, respectively. Errors in the composition of the analyzed fluids are within 5% (Table 2).

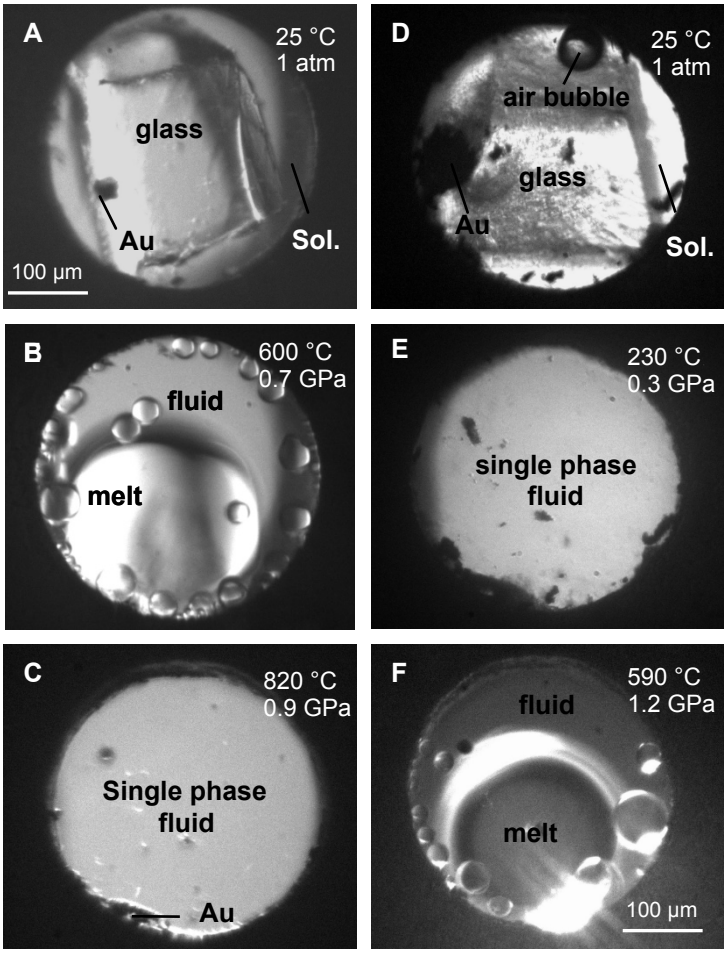
A
25 °C
1 atm
glass
Au
Sol.
100 µm
D
25 °C
1 atm
air bubble
glass
Au
Sol.
B
600 °C
0.7 GPa
fluid
melt
E
230 °C
0.3 GPa
single phase
fluid
C
820 °C
0.9 GPa
Single phase
fluid
Au
F
590 °C
1.2 GPa
fluid
melt
100 µm

Figure 1

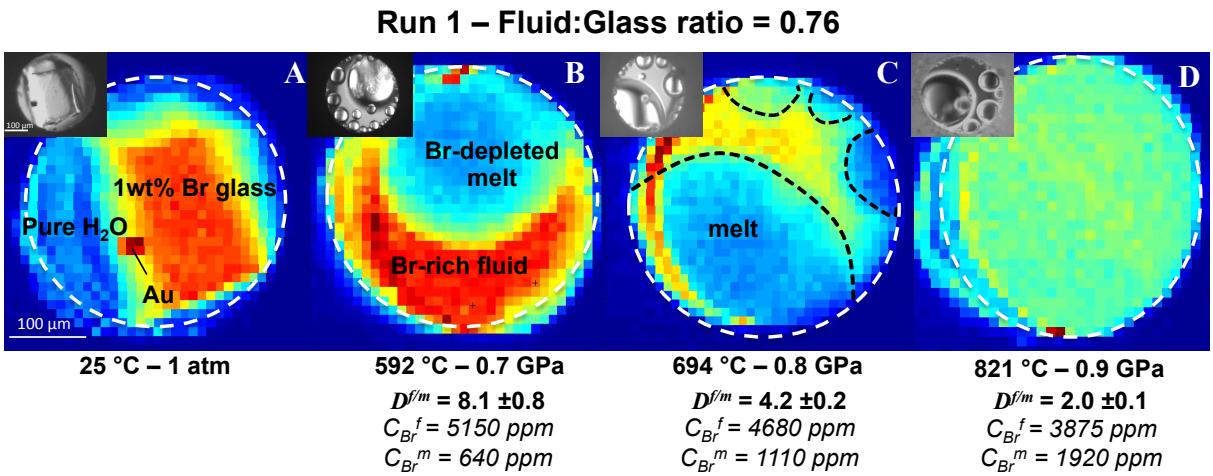
Run 1 – Fluid:Glass ratio = 0.76
A
B
C
D
1wt% Br glass
Pure H2O
Au
100 µm
Br-depleted melt
Br-rich fluid
melt
25 °C – 1 atm
592 °C – 0.7 GPa
D^f/m = 8.1 ±0.8
C_Br^f = 5150 ppm
C_Br^m = 640 ppm
694 °C – 0.8 GPa
D^f/m = 4.2 ±0.2
C_Br^f = 4680 ppm
C_Br^m = 1110 ppm
821 °C – 0.9 GPa
D^f/m = 2.0 ±0.1
C_Br^f = 3875 ppm
C_Br^m = 1920 ppm

Figure 2

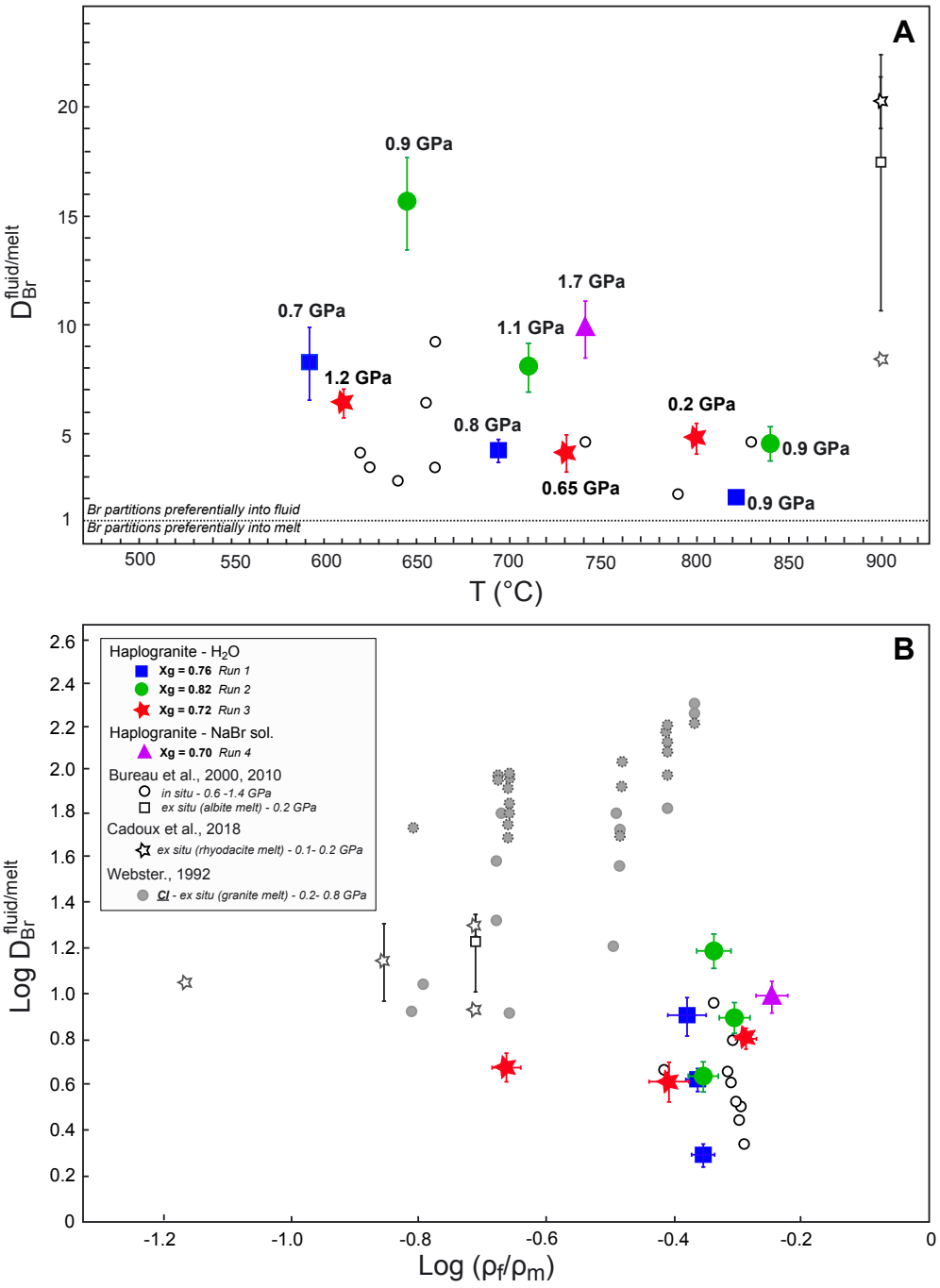
A
0.9 GPa
0.7 GPa
1.7 GPa
1.1 GPa
1.2 GPa
0.2 GPa
0.8 GPa
0.9 GPa
0.65 GPa
0.9 GPa
Br partitions preferentially into fluid
Br partitions preferentially into melt
D fluid/melt Br
T (°C)
B
Haplogranite - H2O
Xg = 0.76 Run 1
Xg = 0.82 Run 2
Xg = 0.72 Run 3
Haplogranite - NaBr sol.
Xg = 0.70 Run 4
Bureau et al., 2000, 2010
in situ - 0.6 -1.4 GPa
ex situ (albite melt) - 0.2 GPa
Cadoux et al., 2018
ex situ (rhyodacite melt) - 0.1- 0.2 GPa
Webster., 1992
Cl - ex situ (granite melt) - 0.2- 0.8 GPa
Log D fluid/melt Br
Log (ρf/ρm)

Figure 3

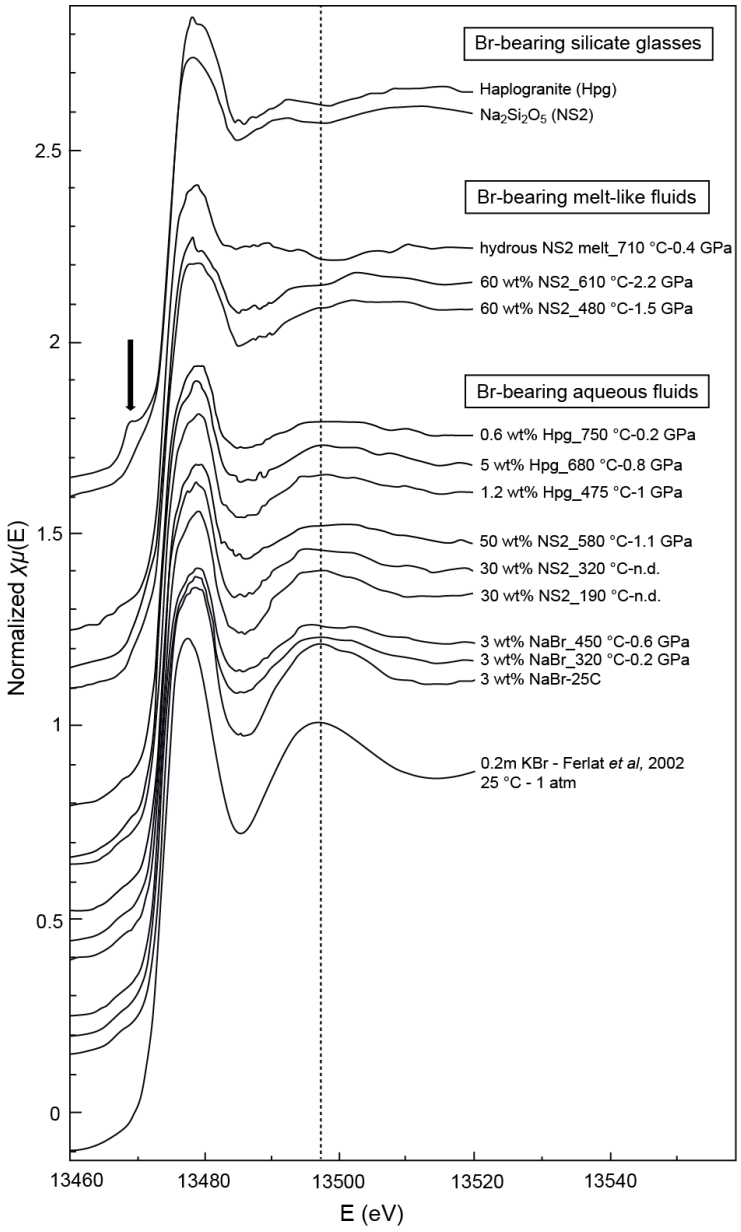
Br-bearing silicate glasses
Haplogranite (Hpg)
Na2Si2O5 (NS2)
Br-bearing melt-like fluids
hydrous NS2 melt_710 °C-0.4 GPa
60 wt% NS2_610 °C-2.2 GPa
60 wt% NS2_480 °C-1.5 GPa
Br-bearing aqueous fluids
0.6 wt% Hpg_750 °C-0.2 GPa
5 wt% Hpg_680 °C-0.8 GPa
1.2 wt% Hpg_475 °C-1 GPa
50 wt% NS2_580 °C-1.1 GPa
30 wt% NS2_320 °C-n.d.
30 wt% NS2_190 °C-n.d.
3 wt% NaBr_450 °C-0.6 GPa
3 wt% NaBr_320 °C-0.2 GPa
3 wt% NaBr-25C
0.2m KBr - Ferlat et al, 2002
25 °C - 1 atm
Normalized χμ(E)
E (eV)
0
0.5
1
1.5
2
2.5
13460
13480
13500
13520
13540

Figure 4

970

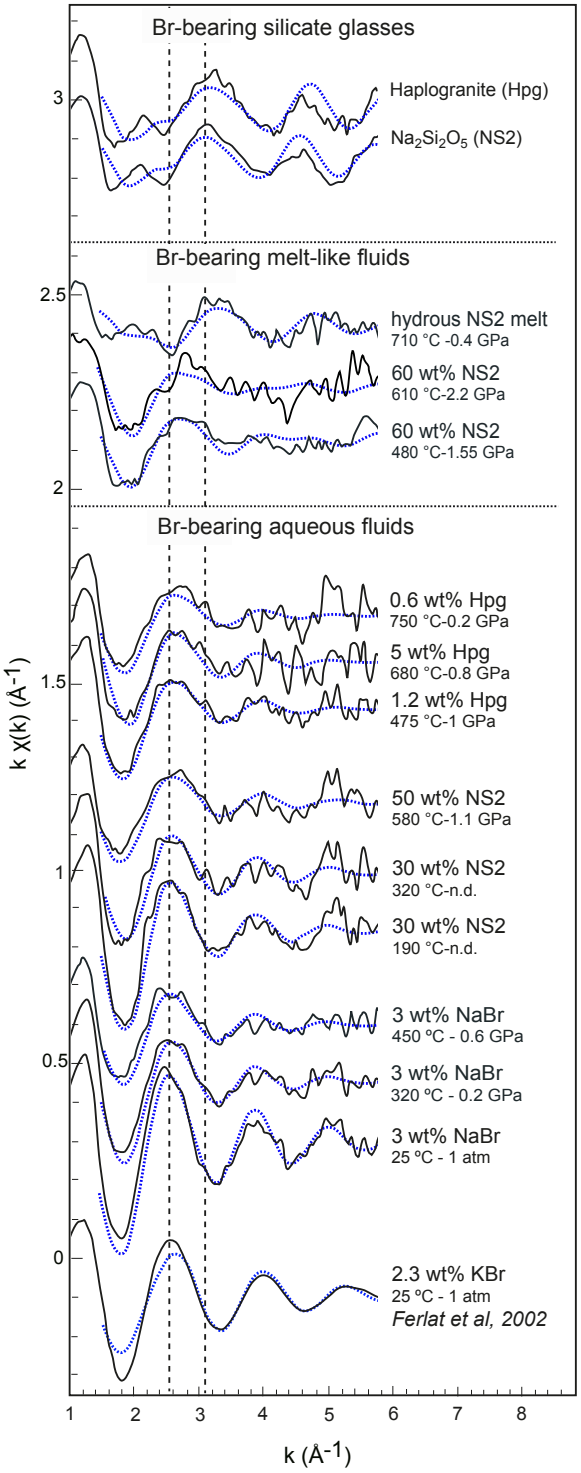

971

972 **Figure 5**

973

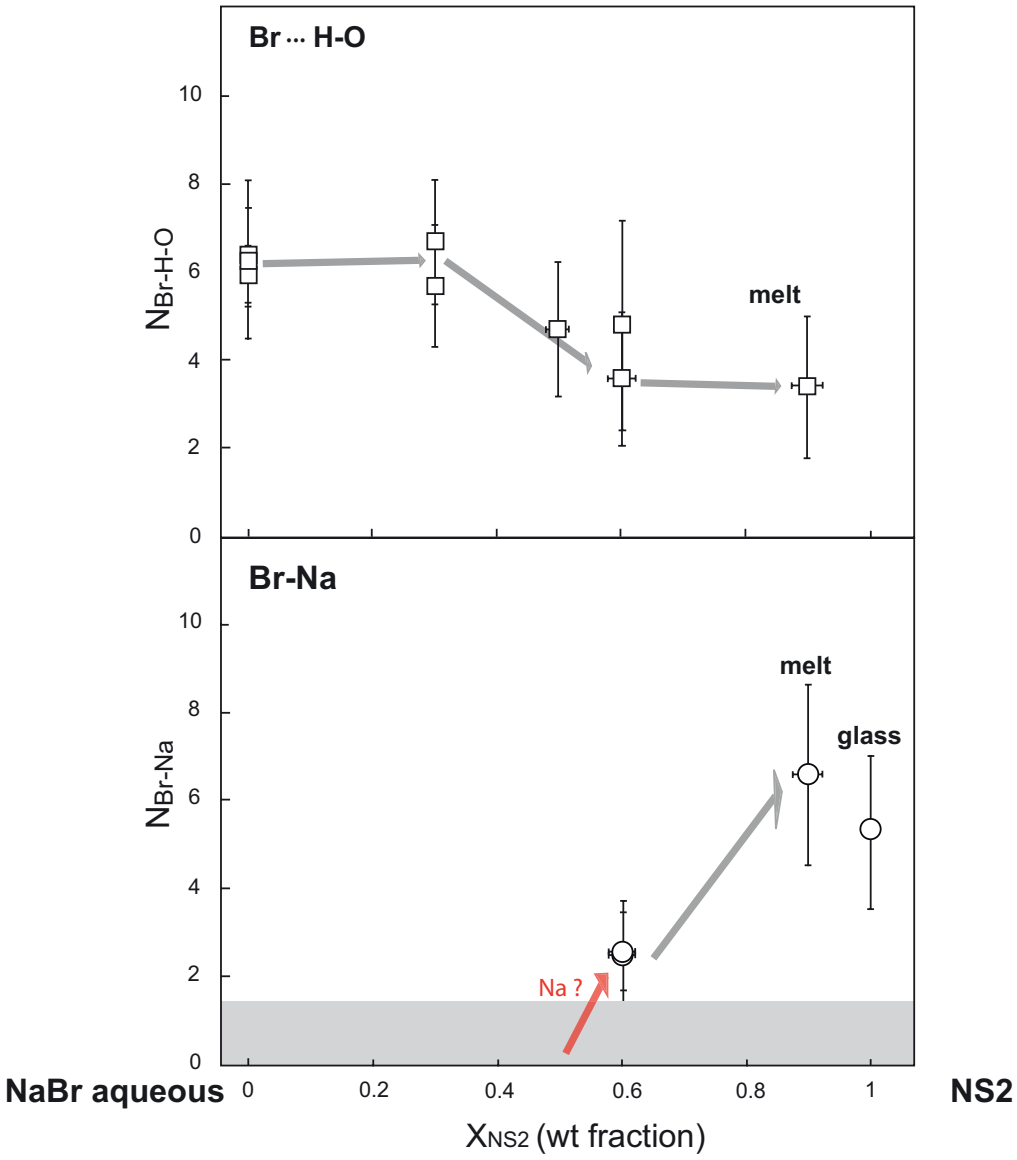

974

975

976 **Figure 6**